

# Approximate Message Passing with a Colored Aliasing Model for Variable Density Fourier Sampled Images

Charles Millard, *Student Member, IEEE*, Aaron T Hess, Boris Mailhé and Jared Tanner, *Member, IEEE*

The Approximate Message Passing (AMP) algorithm efficiently reconstructs signals which have been sampled with large i.i.d. sub-Gaussian sensing matrices. However, when Fourier coefficients of a signal with non-uniform spectral density are sampled, such as in Magnetic Resonance Imaging (MRI), the aliasing is intrinsically colored. Consequently, AMP's i.i.d. state evolution is no longer accurate and the algorithm encounters convergence problems. In response, we propose an algorithm based on Orthogonal Approximate Message Passing (OAMP) that uses the wavelet domain to model the colored aliasing. We present empirical evidence that a structured state evolution occurs, where the effective noise covariance matrix is diagonal with one unique entry per subband. A benefit of state evolution is that Stein's Unbiased Risk Estimate (SURE) can be effectively implemented, yielding an algorithm with no free parameters. We empirically evaluate the effectiveness of the parameter-free algorithm on a synthetic image with three variable density sampling schemes and find that it converges in over 20x fewer iterations than optimally tuned Fast Iterative Shrinkage-Thresholding (FISTA).

**Index Terms**—Approximate Message Passing, Compressed Sensing, Magnetic Resonance Imaging (MRI), Stein's Unbiased Risk Estimate, Variable Density Sampling

## I. INTRODUCTION

WE consider a complex data vector  $\mathbf{y} \in \mathbb{C}^N$  formed of noisy Fourier coefficients of a signal of interest  $\mathbf{x}_0 \in \mathbb{C}^N$ :

$$\mathbf{y} = \mathbf{M}_\Omega(\mathbf{F}\mathbf{x}_0 + \varepsilon), \quad (1)$$

where  $\mathbf{F}$  is a multi-dimensional discrete Fourier transform and  $\mathbf{M}_\Omega \in \mathbb{R}^{N \times N}$  is a diagonal undersampling mask with 1 on the  $j$ th diagonal entry if  $j \in \Omega$  and 0 otherwise, where  $\Omega$  is a sampling set with  $|\Omega| = n$  for  $n < N$ . Here,  $\varepsilon \sim \mathcal{CN}(\mathbf{0}, \sigma_\varepsilon^2 \mathbf{1}_N)$  where  $\mathbf{1}_N$  is the  $N \times N$  identity matrix and  $\mathcal{CN}(\boldsymbol{\mu}, \boldsymbol{\Sigma}^2)$  denotes the distribution with independent real and imaginary parts that are normally distributed with mean  $\boldsymbol{\mu}$  and covariance matrix  $\boldsymbol{\Sigma}^2/2$ . A well-studied approach is to seek a solution of

$$\hat{\mathbf{x}} = \underset{\mathbf{x} \in \mathbb{C}^N}{\operatorname{argmin}} \frac{1}{2} \|\mathbf{y} - \mathbf{M}_\Omega \mathbf{F} \mathbf{x}\|_2^2 + f(\mathbf{x}) \quad (2)$$

where  $f(\mathbf{x})$  is a model-based penalty function. Compressed sensing [7], [9] concerns the reconstruction of signals of interest from underdetermined measurements, where sparsity in  $\hat{\mathbf{x}}$  is promoted by solving (2) with  $f(\mathbf{x}) = \lambda \|\boldsymbol{\Psi} \mathbf{x}\|_1$  for sparse weighting  $\lambda > 0$  and sparsifying transform  $\boldsymbol{\Psi}$ .

A prominent success of compressed sensing with Fourier measurements is accelerated Magnetic Resonance Imaging (MRI) [10], [18], [23], [28], [41], where the signal of interest

$\mathbf{x}_0$  is a natural image. Images of interest typically have a highly non-uniform spectral density that is concentrated at low frequencies. Accordingly, it is well-known that better image restoration is possible if the sampling set  $\Omega$  is generated with variable density, so that there is a higher probability of sampling low frequencies [8], [21], [32], [39]. This work considers an  $\Omega$  with elements drawn independently from a Bernoulli distribution with generic non-uniform probability, so that  $\operatorname{Prob}(j \in \Omega) = p_j \in [0, 1]$ .

### A. Approximate Message Passing

The Approximate Message Passing (AMP) algorithm [12] is an iterative method that, for certain sensing matrices  $\boldsymbol{\Phi} \in \mathbb{C}^{n \times N}$ , efficiently estimates  $\mathbf{x}_0$  in problems of the form  $\mathbf{y} = \boldsymbol{\Phi} \mathbf{x}_0 + \varepsilon$ . At iteration  $k$ , AMP implements a denoiser  $\mathbf{g}(\mathbf{r}_k; \tau_k)$  on  $\mathbf{r}_k$  with mean-squared error estimate  $\tau_k$ . For instance, for penalty function  $f(\mathbf{x})$ ,  $\mathbf{g}(\mathbf{r}_k; \tau_k)$  is the proximal operator associated with  $f(\mathbf{x})$ :

$$\mathbf{g}(\mathbf{r}_k; \tau_k) = \underset{\mathbf{x} \in \mathbb{C}^N}{\operatorname{argmin}} \frac{1}{2\tau_k} \|\mathbf{r}_k - \mathbf{x}\|_2^2 + f(\mathbf{x}), \quad (3)$$

which is equal to soft thresholding in the case of  $f(\mathbf{x}) = \lambda \|\boldsymbol{\Psi} \mathbf{x}\|_1$  and orthogonal  $\boldsymbol{\Psi}$ . For certain sensing matrices and given mild conditions on  $f(\mathbf{x})$ , AMP's state evolution guarantees that in the large system limit  $n, N \rightarrow \infty$ ,  $n/N \rightarrow \delta \in (0, 1)$ , vector  $\mathbf{r}_k$  is the original signal corrupted by zero-mean complex Gaussian noise with a covariance matrix that is proportional to the identity:

$$\mathbf{r}_k = \mathbf{x}_0 + \mathcal{CN}(\mathbf{0}, \sigma_k^2 \mathbf{1}_N) \quad (4)$$

where  $\sigma_k$  is a scalar iteration-dependant standard deviation. When the covariance matrix is proportional to the identity, as in (4), the noise and state evolution are referred to in this work as *white*. The white state evolution of AMP has been proven for real i.i.d. Gaussian measurements in [4] and i.i.d. sub-Gaussian measurements in [3]. It has also been shown empirically that it holds for uniformly undersampled

Manuscript submitted for review on 13th March 2020. A preliminary form of this manuscript was submitted to the IEEE International Conference on Image Processing 2020: see [26]. This work was supported by an EPSRC Industrial CASE studentship with Siemens Healthineers, voucher number 17000051, and by The Alan Turing Institute under the EPSRC grant EP/N510129/1. The concepts and information presented in this paper are based on research results that are not commercially available.

Charles Millard and Jared Tanner are with the Mathematical Institute at the University of Oxford, Oxford, OX2 6GG, UK (e-mail: millard@maths.ox.ac.uk; tanner@maths.ox.ac.uk)

Aaron T Hess is with the Oxford Centre for Clinical Magnetic Resonance at the University of Oxford, Oxford, OX3 9DU, UK (e-mail: aaron.hess@cardiov.ox.ac.uk)

Boris Mailhé is with Siemens Healthineers, 755 College Rd E, Princeton, NJ 08540, USA (e-mail: boris.mailhe@siemens-healthineers.com)

Fourier measurements of an artificial i.i.d. signal [12]. When state evolution holds, AMP is known to exhibit very fast convergence. However, for generic  $\Phi$ , the behavior of AMP is not well understood and it has been noted by a number of authors [6], [17], [33], [35] that it can encounter convergence problems. The recent Orthogonal AMP (OAMP) [24] and related Vector Approximate Message Passing (VAMP) [34] algorithm obey a white state evolution for a broader class of measurement matrices  $\Phi$ , and were found to perform very well on certain reconstruction tasks. For VAMP, white state evolution was proven for sensing matrices that are ‘right-orthogonally invariant’: see [34] for details.

### B. Colored aliasing

AMP, OAMP and VAMP assume that the entries of  $\mathbf{x}_0$  are i.i.d. and that the sensing matrix is sufficiently random to ensure that the aliasing is white. However, when an image is sampled in the Fourier domain the aliasing is innately colored. To see this, consider the natural initialization for an approximate message passing algorithm: the unbiased estimator  $\tilde{\mathbf{x}} = \mathbf{F}^H \mathbf{P}^{-1} \mathbf{y}$ , where  $\mathbf{P}$  is the diagonal matrix formed from sampling probabilities  $p_j$ . Denoting  $\mathbf{y}_0 = \mathbf{F} \mathbf{x}_0$ , the power spectrum of the aliasing of  $\tilde{\mathbf{x}}$  is

$$\mathbb{E}_{\Omega, \varepsilon} \{ |\mathbf{y}_0 - \mathbf{P}^{-1} \mathbf{y}|^2 \} = \mathbb{E}_{\Omega, \varepsilon} \{ |\mathbf{y}_0 - \mathbf{P}^{-1} \mathbf{M}_{\Omega}(\mathbf{y}_0 + \varepsilon)|^2 \} \quad (5a)$$

$$= \mathbb{E}_{\varepsilon} \{ |\mathbf{P} \mathbf{y}_0 - \mathbf{P}^{-1}(\mathbf{y}_0 + \varepsilon)|^2 + (\mathbf{1}_N - \mathbf{P}) |\mathbf{y}_0|^2 \} \quad (5b)$$

$$= (\mathbf{P}^{-1} - \mathbf{1}_N) |\mathbf{y}_0|^2 + \sigma_{\varepsilon}^2 \mathbf{P}^{-1} \mathbf{1}_N \quad (5c)$$

where  $|\cdot|^2$  is the entry-wise absolute squared and  $\mathbf{1}_N$  is the  $N$ -dimensional vector of ones. Equation (5) depends on  $\mathbf{P}$  and  $|\mathbf{y}_0|^2$ , which are non-uniform and anisotropic in general. Note that although the specific case  $p_j = (\sigma_{\varepsilon}^2 + |y_{0,j}|^2)/(\alpha + |y_{0,j}|^2)$  for constant  $\alpha$  does lead to white aliasing, it requires knowledge of the ground truth spectral density so is not feasible in practice.

A visual example of colored aliasing is shown in the top row of Fig. 1. Here, the unbiased estimate of a 512x512 synthetic Shepp-Logan uniformly sampled with  $p_j = 1/2$  for all  $j$  is shown, with  $\sigma_{\varepsilon} = 0$ . The power spectrum of the aliasing is proportional to the power spectrum of the signal, so is highly colored. Sampling with variable density can partially but not entirely compensate for the power spectrum of the signal.

The intrinsically colored aliasing of variable density sampling from a non-uniform spectral density implies that the white state evolution of AMP, (4), is not feasible. The primary development of this work is based on the use of the Discrete Wavelet Transform (DWT) to compute a multiresolution decomposition of the power spectrum of the aliasing [15], [19]. In the wavelet domain colored aliasing has a structure that resembles a state evolution. To illustrate this, consider again the unbiased initialization  $\tilde{\mathbf{x}}$ . The corresponding estimator in the wavelet domain is

$$\mathbf{r}_0 = \Psi \tilde{\mathbf{x}}. \quad (6)$$

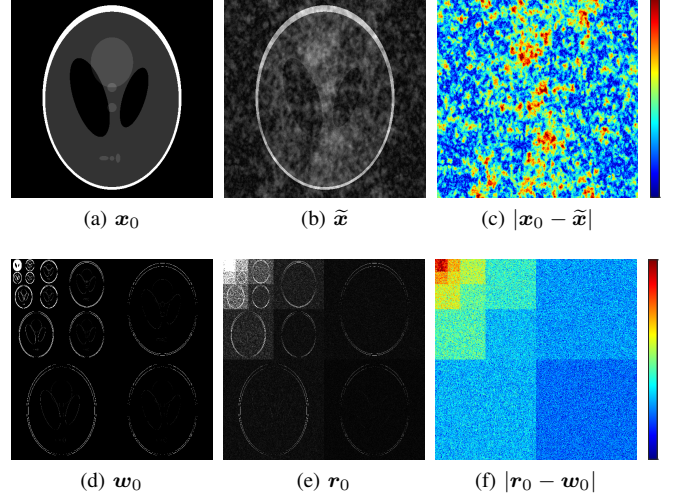


Fig. 1: The ground truth, unbiased estimate and entry-wise absolute error for a uniformly sampled Shepp-Logan with  $p_j = 1/2$ . The top row shows the image domain and the bottom shows the wavelet domain. The colored aliasing evident in Fig. 1c illustrates the infeasibility of white state evolution for Fourier sampling of signals with non-uniform spectral density. For visualization, Fig. 1f shows the entry-wise logarithm. The anisotropy of the spectral density of  $\mathbf{x}_0$  causes the horizontal, vertical and diagonal variances to differ, even at the same scale.

The bottom row of Fig. 1 shows  $\mathbf{w}_0 = \Psi \mathbf{x}_0$ ,  $\mathbf{r}_0$  and the entry-wise absolute difference  $|\mathbf{w}_0 - \mathbf{r}_0|$  for the same image and sampling set as the top row, where  $\Psi$  is a Haar wavelet with 4 decomposition scales. Fig. 1f indicates that the power spectrum given by (5) has a simple structure in the wavelet domain; in particular, *each wavelet subband behaves as the ground truth subband corrupted by zero-mean white Gaussian noise*. The variance of the Gaussian noise depends on the power spectrum of the aliasing and is different for each subband.

### C. Colored state evolution

Herein we present a new method for undersampled signal reconstruction that we term the Variable Density Approximate Message Passing (VDAMP) algorithm, see Algorithm 1. We present empirical evidence that VDAMP preserves the subband-dependent noise structure illustrated in Fig. 1f for all iterations. Explicitly, the  $\mathbf{r}_k$  of VDAMP behaves as

$$\mathbf{r}_k = \mathbf{w}_0 + \mathcal{CN}(\mathbf{0}, \Sigma_k^2), \quad (7)$$

where  $\Psi$  is an orthogonal DWT and the covariance matrix  $\Sigma_k^2$  is diagonal so that for a  $\Psi$  with  $s$  decomposition scales

$$\Sigma_k^2 = \begin{bmatrix} \sigma_{k,1}^2 \mathbf{1}_{N_1} & 0 & \dots & 0 \\ 0 & \sigma_{k,2}^2 \mathbf{1}_{N_2} & \dots & 0 \\ \vdots & \vdots & \ddots & \vdots \\ 0 & 0 & \dots & \sigma_{k,1+3s}^2 \mathbf{1}_{N_{1+3s}} \end{bmatrix}, \quad (8)$$

where  $\sigma_{k,b}^2$  and  $N_b$  refer to the variance and dimension of the  $b$ th subband respectively. We refer to (7) and (8) as the *colored state evolution* of VDAMP and  $\mathbf{r}_k - \mathbf{w}_0$  as the *effective noise* of VDAMP. To our knowledge, VDAMP is the first algorithm for variable density Fourier sampling of natural images where a state evolution has been observed.

The joint time-frequency localization provided by the wavelet transform decomposes the color of the effective noise while retaining incoherence. In the numerical examples presented in Section III a sparse model on wavelet coefficients is considered, however, we emphasize that VDAMP uses the wavelet transform only as a tool for decomposing the aliasing, and is not constrained to models directly on wavelet coefficients [25], [40].

## II. DESCRIPTION OF ALGORITHM

The VDAMP algorithm is stated in Algorithm 1, where  $|\cdot|$  is the entry-wise absolute value of a vector or matrix and  $\odot$  is entry-wise multiplication. The effective noise covariance matrix is represented by a *vector*  $\boldsymbol{\tau}_k \in \mathbb{R}^N$  that models the diagonal of (7). The function  $\mathbf{g}(\mathbf{r}_k; \boldsymbol{\tau}_k)$  is a denoiser with a colored effective noise model  $\boldsymbol{\tau}_k$ . The notation  $\partial(\mathbf{g}(\mathbf{r}_k; \boldsymbol{\tau}_k))$  in line 7 of Algorithm 1 is defined as the function with  $j$ th entry

$$\partial_j(\mathbf{g}(\mathbf{r}_k; \boldsymbol{\tau}_k)) = \frac{1}{2} \left( \frac{\partial \Re[g_j(\mathbf{r}_k; \boldsymbol{\tau}_k)]}{\partial \Re[r_j]} + \frac{\partial \Im[g_j(\mathbf{r}_k; \boldsymbol{\tau}_k)]}{\partial \Im[r_j]} \right) \quad (9)$$

where  $\Re[\cdot]$  and  $\Im[\cdot]$  are the real and imaginary parts respectively. In line 7, the notation  $\langle \cdot \rangle_{\text{sband}}$  is an operator that empirically averages over subbands, so that  $\boldsymbol{\alpha}_k$  has the structure

$$\boldsymbol{\alpha}_k = \begin{bmatrix} \alpha_{k,1} \mathbf{1}_{N_1} \\ \alpha_{k,2} \mathbf{1}_{N_2} \\ \vdots \\ \alpha_{k,1+3s} \mathbf{1}_{N_{1+3s}} \end{bmatrix} \quad (10)$$

with

$$\alpha_{k,b} = \frac{1}{N_b} \sum_{j \in J_b} \partial_j(\mathbf{g}(\mathbf{r}_k; \boldsymbol{\tau}_k)), \quad (11)$$

where  $J_b$  is the set of indices associated with subband  $b$  and  $N_b = |J_b|$ .

### A. Weighted gradient descent

To ensure that  $\mathbf{r}_k$  is an unbiased estimate of  $\mathbf{x}_0$ , the sensing matrix must be correctly normalized. In VDAMP this is manifest in the gradient step of lines 3-4, which features a crucial weighting by  $\mathbf{P}^{-1}$  that is absent in previous applications of AMP to variable density sampling [13], [38], where a state evolution was not observed. This provides the correct normalisation in expectation over  $\Omega$ :  $\mathbb{E}_\Omega\{\Psi \mathbf{F}^H \mathbf{P}^{-1} \mathbf{M}_\Omega \mathbf{F} \Psi^H\} = \mathbf{1}_N$ , which implies that  $\mathbb{E}_{\Omega, \varepsilon}\{\mathbf{r}_k\} = \mathbf{w}_0$  for all  $k$ . VDAMP's  $\mathbf{r}_0$  is the unbiased estimator from (6). Such a rescaling is referred to as ‘density compensation’ in the MRI literature [29], [30], and was used in the original compressed sensing MRI paper with zero-filling to generate a unregularized, non-iterative baseline [23].

### Algorithm 1 VDAMP

**Require:** Sampling set  $\Omega$ , wavelet transform  $\Psi$ , probability matrix  $\mathbf{P}$ , measurements  $\mathbf{y}$ , denoiser  $\mathbf{g}(\mathbf{r}_k; \boldsymbol{\tau}_k)$ , number of iterations  $K_{it}$ .

```

1: Set  $\tilde{\mathbf{r}}_0 = \mathbf{0}$  and compute  $\mathbf{S} = |\mathbf{F} \Psi^H|^2$ 
2: for  $k = 0, 1, \dots, K_{it} - 1$  do
3:    $\mathbf{z}_k = \mathbf{y} - \mathbf{M}_\Omega \mathbf{F} \Psi^H \tilde{\mathbf{r}}_k$ 
4:    $\mathbf{r}_k = \tilde{\mathbf{r}}_k + \Psi \mathbf{F}^H \mathbf{P}^{-1} \mathbf{z}_k$ 
5:    $\boldsymbol{\tau}_k = \mathbf{S}^H \mathbf{M}_\Omega \mathbf{P}^{-1} [(\mathbf{P}^{-1} - \mathbf{1}_N) |\mathbf{z}_k|^2 + \sigma_\varepsilon^2 \mathbf{1}_N]$ 
6:    $\hat{\mathbf{w}}_k = \mathbf{g}(\mathbf{r}_k; \boldsymbol{\tau}_k)$ 
7:    $\boldsymbol{\alpha}_k = \langle \partial(\mathbf{g}(\mathbf{r}_k; \boldsymbol{\tau}_k)) \rangle_{\text{sband}}$ 
8:   Update  $\mathbf{c}_k$ 
9:    $\tilde{\mathbf{r}}_{k+1} = \mathbf{c}_k \odot (\hat{\mathbf{w}}_k - \boldsymbol{\alpha}_k \odot \mathbf{r}_k)$ 
10: end for
11: return  $\hat{\mathbf{x}} = \Psi^H \hat{\mathbf{w}}_k + \mathbf{F}^H (\mathbf{y} - \mathbf{M}_\Omega \mathbf{F} \Psi^H \hat{\mathbf{w}}_k)$ 

```

Scaling by  $\mathbf{P}^{-1}$  increases the variance of the measurement noise at frequencies sampled with low probability, and its inclusion in the gradient step will lead to a  $\mathbf{r}_k$  with higher mean-squared error than an unweighted gradient step. However, as shown in Section III, a careful choice of denoiser  $\mathbf{g}(\mathbf{r}_k; \boldsymbol{\tau}_k)$  that leverages VDAMP's state evolution can cause lines 6-9 to be very effective, leading to faster overall convergence than competing methods.

The final step of VDAMP, line 11, is a gradient step without a  $\mathbf{P}^{-1}$  weighting, which generates a biased image estimate  $\hat{\mathbf{x}}$  with high data fidelity.

### B. Colored effective noise model

Line 5 of Algorithm 1 computes an estimate of the colored effective noise covariance matrix  $\Sigma_k^2$  from (7). Through a similar calculation to (5), the power spectrum of the aliasing of  $\mathbf{r}_k$  is

$$\mathbb{E}_{\Omega, \varepsilon}\{|\mathbf{F} \Psi^H \mathbf{r}_k - \mathbf{y}_0|^2\} = (\mathbf{P}^{-1} - \mathbf{1}_N) |\mathbf{F} \Psi^H \tilde{\mathbf{r}}_k - \mathbf{y}_0|^2 + \sigma_\varepsilon^2 \mathbf{P}^{-1} \mathbf{1}_N. \quad (12)$$

Using importance sampling with importance distribution  $\mathbf{P}$ , an unbiased estimate of (12) that does not require knowledge of the ground truth is

$$\boldsymbol{\tau}_k^y = \mathbf{M}_\Omega \mathbf{P}^{-1} [(\mathbf{P}^{-1} - \mathbf{1}_N) |\mathbf{z}_k|^2 + \sigma_\varepsilon^2 \mathbf{1}_N]. \quad (13)$$

The computation of  $\boldsymbol{\tau}_k$  in line 5 of Algorithm 1 is a linear transform of  $\boldsymbol{\tau}_k^y$  to the wavelet domain.  $\mathbf{S}$  is the power spectrum of  $\Psi$ , so has  $1 + 3s$  unique columns; line 5 therefore requires  $1 + 3s$  inner products. We assume the estimator  $\boldsymbol{\tau}_k$  concentrates around its expectation, and leave the study of the constraints this imposes on  $\mathbf{P}$  for future works. Note that for fixed  $s$  the complexity of VDAMP is governed by  $\Psi$  and  $\mathbf{F}$ , whose fast implementations have complexity  $O(N \log N)$ .

### C. Orthogonality between errors

This section motivates the form of lines 6-9 of Algorithm 1. Consider the function formed by merging these lines:

$$\tilde{\mathbf{g}}(\mathbf{r}_k; \boldsymbol{\tau}_k) = \mathbf{c}_k \odot (\mathbf{g}(\mathbf{r}_k; \boldsymbol{\tau}_k) - \boldsymbol{\alpha}_k \odot \mathbf{r}_k). \quad (14)$$

In the following we show that when  $\mathbf{r}_k$  behaves as (7), this construction establishes approximate orthogonality between error vectors  $\mathbf{r}_k - \mathbf{w}_0$  and  $\tilde{\mathbf{g}}(\mathbf{r}_k; \boldsymbol{\tau}_k) - \mathbf{w}_0$ . Orthogonality between errors is used in OAMP as a non-rigorous alternative to independence between errors, a requirement for state evolution; see [24] for details.

Consider a random variable  $\mathbf{R}_k = \mathbf{w}_0 + \boldsymbol{\Sigma}_k \mathbf{Z}$  where  $\mathbf{Z} \sim \mathcal{CN}(\mathbf{0}, \mathbf{1}_N)$  and  $\boldsymbol{\Sigma}_k^2$  is defined in (8). Since  $\mathbb{E}_{\mathbf{Z}}\{\mathbf{Z}\} = \mathbf{0}$ ,

$$\begin{aligned} \mathbb{E}_{\mathbf{R}_k}\{(\mathbf{R}_k - \mathbf{w}_0)^H (\tilde{\mathbf{g}}(\mathbf{R}_k; \boldsymbol{\tau}_k) - \mathbf{w}_0)\} \\ = \mathbb{E}_{\mathbf{R}_k}\{(\mathbf{R}_k - \mathbf{w}_0)^H \tilde{\mathbf{g}}(\mathbf{R}_k; \boldsymbol{\tau}_k)\}, \end{aligned} \quad (15)$$

which, by Stein's Lemma [14], [36], is

$$(15) = \mathbb{E}_{\mathbf{R}_k} \left\{ \frac{1}{2} \sum_j \boldsymbol{\Sigma}_{k,jj}^2 \left( \frac{\partial \Re[\tilde{g}_j(\mathbf{R}_k; \boldsymbol{\tau}_k)]}{\partial \Re[R_{k,j}]} + i \frac{\partial \Im[\tilde{g}_j(\mathbf{R}_k; \boldsymbol{\tau}_k)]}{\partial \Im[R_{k,j}]} \right) \right\}, \quad (16)$$

where the factor of  $\frac{1}{2}$  arises due to the  $\boldsymbol{\Sigma}_k^2/2$  covariance matrix of the real and imaginary parts of  $\mathbf{Z}$ . If VDAMP's  $\mathbf{r}_k$  are instances of the random variable  $\mathbf{R}_k$ ,  $\boldsymbol{\alpha}_k$  is an estimate of  $\mathbb{E}_{\mathbf{R}_k}\{\langle \partial(\mathbf{g}(\mathbf{R}_k; \boldsymbol{\tau}_k)) \rangle_{\text{sband}}\}$ , and the right-hand side of (16) is approximately zero. Therefore, for large  $N$ ,

$$(\mathbf{r}_k - \mathbf{w}_0)^H (\tilde{\mathbf{g}}(\mathbf{r}_k; \boldsymbol{\tau}_k) - \mathbf{w}_0) \approx 0. \quad (17)$$

Note that this property holds for arbitrary  $c_k$ . Two choices for  $c_k$  are discussed in III-B.

### III. NUMERICAL EXPERIMENTS

This section illustrates the performance of VDAMP compared with the Fast Iterative Shrinking-Thresholding Algorithm (FISTA) algorithm [5] and a parameter-free method based on FISTA [20], and presents empirical evidence for VDAMP's state evolution.

#### A. Complex soft threshold tuning with SURE

Selecting appropriate regularisation parameters such as  $\lambda$  is a notable challenge in real-world compressed sensing applications. We present an approach to parameter-free compressed sensing reconstruction that leverages VDAMP's state evolution by applying Stein's Unbiased Risk Estimate (SURE) [37], building on work on AMP in [16], [27].

A strength of automatic parameter tuning via SURE is that it is possible to have a richer regularizer than would usually be feasible for a hand-tuned  $f(\mathbf{x})$ . In the experiments presented in this section, the denoiser  $\mathbf{g}(\mathbf{r}_k; \boldsymbol{\tau}_k)$  was the complex soft thresholding operator with a subband-dependant threshold that is tuned automatically with SURE. In other words, SURE with a effective noise model given by  $\mathbf{r}_k = \mathbf{w}_0 + \mathcal{CN}(\mathbf{0}, \text{Diag}(\boldsymbol{\tau}_k))$  was used to approximately solve

$$\mathbf{g}(\mathbf{r}_k; \boldsymbol{\tau}_k) \approx \underset{\mathbf{w} \in \mathbb{C}^N}{\text{argmin}} \min_{\boldsymbol{\lambda} \in \mathbb{R}^N} \frac{1}{2} \|(\mathbf{w} - \mathbf{r}_k) \odot \sqrt{\boldsymbol{\tau}_k}\|_2^2 + \|\boldsymbol{\lambda} \odot \mathbf{w}\|_1, \quad (18)$$

where  $\odot$  denotes entry-wise division,  $\sqrt{\boldsymbol{\tau}_k}$  is the entry-wise square root of  $\boldsymbol{\tau}_k$  and  $\boldsymbol{\lambda}$  has the structure of (10).

Equation (18) was solved using a procedure related to SureShrink [11] but for Gaussian noise that is complex and colored [19]. Consider a vector  $\mathbf{v}_0 \in \mathbb{C}^{N_v}$  corrupted by white complex Gaussian noise:  $\mathbf{v} = \mathbf{v}_0 + \mathcal{CN}(\mathbf{0}, \tau_v \mathbf{1}_{N_v})$ . Let  $\mathbf{d}(\mathbf{v}) = \mathbf{v} + \mathbf{h}(\mathbf{v})$  be an estimator of  $\mathbf{v}_0$ . SURE for complex variables has the form

$$cSURE(\mathbf{d}(\mathbf{v})) = \|\mathbf{h}(\mathbf{v})\|_2^2 + N_v \tau_v [2 \langle \partial(\mathbf{d}(\mathbf{v})) \rangle - 1], \quad (19)$$

where  $\langle \cdot \rangle$  is the empirical averaging operator. cSURE is an unbiased estimate of the risk:

$$\mathbb{E}\{cSURE(\mathbf{d}(\mathbf{v}))\} = \|\mathbf{d}(\mathbf{v}) - \mathbf{v}_0\|_2^2. \quad (20)$$

Consider the case where  $\mathbf{d}(\mathbf{v})$  is the complex soft thresholding operator  $\boldsymbol{\eta}(\mathbf{v})$  with threshold  $t$ , which acts component-wise as

$$\eta_j(v_j) := v_j \left( 1 - \min \left\{ \frac{t}{|v_j|}, 1 \right\} \right). \quad (21)$$

In this case, (19) is

$$\begin{aligned} cSURE(\boldsymbol{\eta}(\mathbf{v})) &= (t^2 + 2\tau_v) \cdot \#\{i : |v_i| > t\} - N_v \tau_v \\ &+ \sum_{j: |v_j| \leq t} |v_j|^2 + \sum_{j: |v_j| > t} t \tau_v / |v_j|. \end{aligned} \quad (22)$$

In the following experiments the optimal threshold for each subband was estimated with

$$\hat{t} = \underset{t}{\text{argmin}} (cSURE(\boldsymbol{\eta}(\mathbf{v}))) \quad (23)$$

by evaluating (22) for trial thresholds  $t = |v_1|, |v_2|, \dots, |v_{N_v}|$ . For large dimension  $N_v$  one would expect by the law of large numbers that cSURE is close to the true risk, and for the threshold to be almost optimal. Since a larger number of decomposition scales  $s$  give subbands with lower dimensionality, there is a trade-off between the size of  $s$  and the quality of threshold selection with cSURE.

SURE has previously been employed for parameter-free compressed sensing MRI in [20], where FISTA was used with (18) in place of the usual shrinkage step. This algorithm is herein referred to as SURE-IT. The iteration-by-iteration error of SURE-IT is highly non-Gaussian, so deviates from a proper theoretical basis for using SURE and does not give near-optimal threshold selection.

#### B. Updating $c_k$

In the experiments in this section two possibilities for the  $c_k$  update in line 8 of Algorithm 1 are considered. First,

$$\mathbf{c}_k^\alpha = \mathbf{1}_N \odot (\mathbf{1}_N - \boldsymbol{\alpha}_k), \quad (24)$$

In this case lines 6-9 of Algorithm 1 are a colored version of the 'denoising' phase of VAMP when written in LMMSE form (see [34], Algorithm 3). VDAMP with  $c_k$  updated with (24) is herein referred to as VDAMP- $\alpha$ .

Secondly, as in [40], we suggest using SURE for a second time to estimate the  $c_k$  that minimises the mean squared error of  $\tilde{\mathbf{r}}_k$ :

$$\mathbf{c}_k^{SURE} \approx \underset{\mathbf{c}}{\text{argmin}} \|\tilde{\mathbf{g}}(\mathbf{r}_k; \boldsymbol{\tau}_k) - \mathbf{w}_0\|_2^2. \quad (25)$$

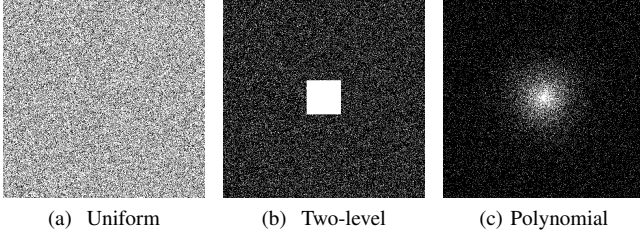


Fig. 3: Sampling set  $\Omega$  for uniform, two-level and polynomial sampling. Low frequencies are at the centre of the image, and a white pixel indicates that the Fourier coefficient was sampled.

Since  $\langle \partial(\tilde{g}(\mathbf{r}_k; \boldsymbol{\tau}_k)) \rangle_{\text{subband}} \approx 0$ , optimizing (19) reduces to a series of  $\ell_2$  minimisation problems with a closed-form solution, so that for the  $b$ th subband

$$\mathbf{c}_{k,b}^{SURE} = \arg \min_{\mathbf{c}} \| \mathbf{c}(\mathbf{g}_b(\mathbf{r}_k; \boldsymbol{\tau}_k) - \alpha_{k,b} \mathbf{r}_{k,b}) - \mathbf{r}_{k,b} \|_2^2 \quad (26a)$$

$$= \frac{\mathbf{r}_{k,b}^H (\mathbf{g}_b(\mathbf{r}_k; \boldsymbol{\tau}_k) - \alpha_{k,b} \mathbf{r}_{k,b})}{\| \mathbf{g}_b(\mathbf{r}_k; \boldsymbol{\tau}_k) - \alpha_{k,b} \mathbf{r}_{k,b} \|_2^2}. \quad (26b)$$

Vector  $\mathbf{c}_k^{SURE}$  is formed from the  $\mathbf{c}_{k,b}^{SURE}$  so that it has the structure of (10). VDAMP with  $\mathbf{c}_k$  updated with  $\mathbf{c}_k^{SURE}$  is herein referred to as VDAMP-S.

### C. Experimental method

We considered the reconstruction of the  $512 \times 512$  Shepp-Logan shown in Fig. 1a. The undersampled data was artificially corrupted with complex Gaussian noise so that  $\| \mathbf{x}_0 \|_2^2 / N \sigma_\varepsilon^2 = 40\text{dB}$ . We assumed that  $\sigma_\varepsilon^2$  was known a priori. A Haar wavelet  $\Psi$  at  $s = 4$  decomposition scales was used. All experiments were conducted in MATLAB 9.4 and can be reproduced with code available at <https://github.com/charlesmillard/VDAMP>.

### D. Comparison with FISTA and SURE-IT

To establish comparative reconstruction quality and convergence speed, VDAMP- $\alpha$  and VDAMP-S were compared with

FISTA and SURE-IT. The scalar sparse weighting  $\lambda$  of FISTA was tuned with an exhaustive search so that the mean-squared error was minimised at  $k = 100$ . FISTA with a fine-tuned subband-dependent  $\lambda$  was not considered as it is not feasible in practise. For SURE-IT the mean-squared error estimate was updated using the ground truth:  $\tau_k = \| \mathbf{w}_0 - \mathbf{r}_k \|_2^2 / N$ , and (18) with  $\boldsymbol{\tau}_k = \tau_k \mathbf{1}_N$  was employed as the denoiser. All algorithms were initialised with a vector of zeros.

Three variable density sampling schemes were considered:

- 1) **Uniform sampling** with  $N/n = 1.5$ .
- 2) **Two-level sampling** with  $p_j = 1$  for a  $42 \times 42$  central region and uniform sampling with  $p_j = 1/6$  otherwise, so that  $N/n = 5$ .
- 3) **Polynomial sampling** generated using the variable density sampling function from the Sparse MRI package<sup>1</sup>, with  $N/n = 12$ .

A visualization of an instance of  $\Omega$  in each case is shown in Fig. 3.

Fig. 2 shows the normalized mean-squared error (NMSE)  $\| \hat{\mathbf{x}} - \mathbf{x}_0 \|_2^2 / \| \mathbf{x}_0 \|_2^2$  versus iteration number for each algorithm for all three sampling sets. VDAMP- $\alpha$  and VDAMP-S were run for  $K_{it} = 50$  iterations, and FISTA and SURE-IT were run for 1000 iterations, except in the uniformly sampled case, where FISTA was run for 10000 iterations. All NMSE values were calculated after an additional data consistency step, as in line 11 of Algorithm 1.

In all cases VDAMP- $\alpha$  and VDAMP-S converge within 50 iterations, illustrating the benefit of iteration-dependant near-optimal regularization that is made feasible by SURE. The comparatively poor performance of SURE-IT highlights the need for zero-mean Gaussian effective noise for effective automatic parameter tuning.

VDAMP- $\alpha$  and VDAMP-S's reduction in required number of iterations is particularly significant in the uniformly sampled case, Fig. 2a, where FISTA did not converge even after 10000 iterations. This reflects the highly colored aliasing that arises when the sampling distribution does not compensate for the

<sup>1</sup>available at <https://people.eecs.berkeley.edu/~mlustig/Software.html>

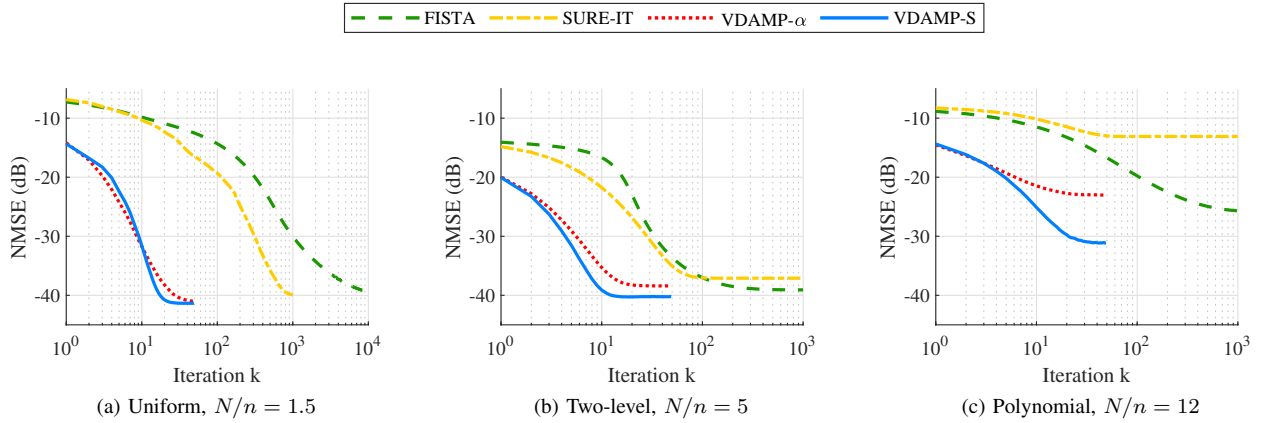


Fig. 2: NMSE of FISTA, SURE-IT, VDAMP- $\alpha$  and VDAMP-S for the three variable density undersampling schemes shown in Fig. 3. The NMSE at  $k = 0$  differs between algorithms as the image estimate at  $k = 0$  is defined to be the after the first thresholding is applied.



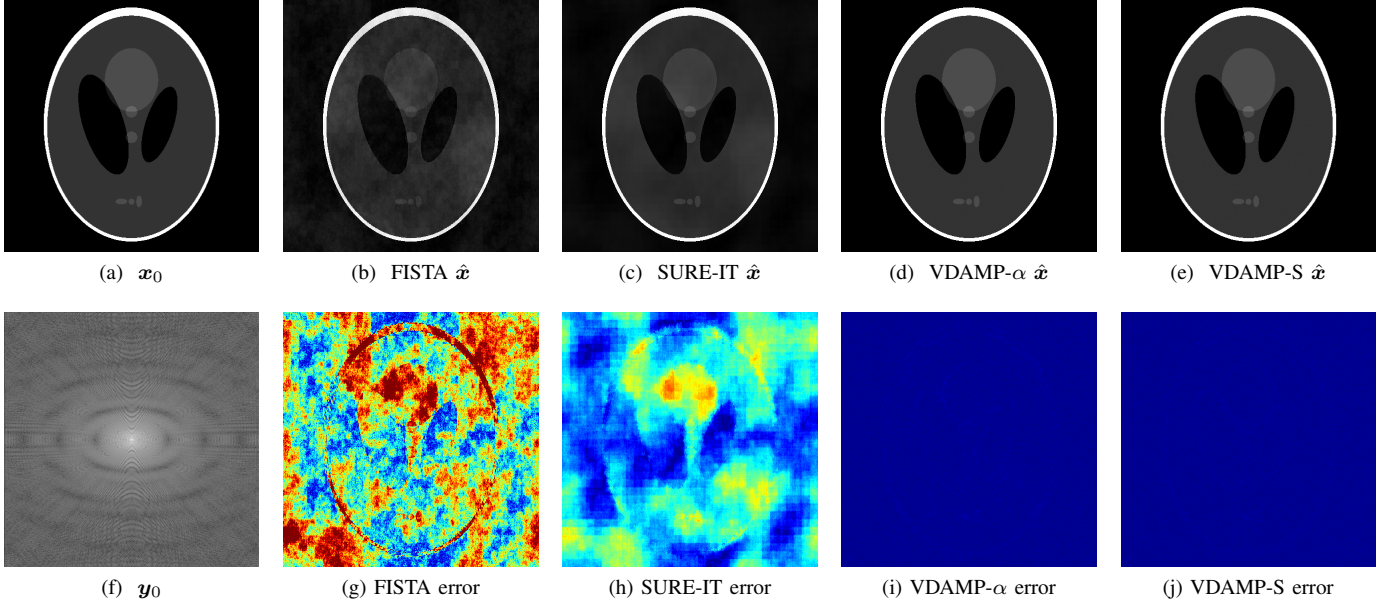


Fig. 4: Uniformly undersampled reconstruction at iteration  $k = 50$  with (b) FISTA (NMSE = -11.9dB) (c) SURE-IT (NMSE = -16.4dB), (d) VDAMP- $\alpha$  (NMSE -41.0dB) and (e) VDAMP-S (NMSE -41.3dB). In all cases the absolute value is shown. For visualization (f) shows the logarithm of  $|\mathbf{y}_0|$ . Figures (g)-(j) show the entry-wise absolute difference  $|\hat{\mathbf{x}} - \mathbf{x}_0|$  and are represented on the same scale. Note the visible undersampling artefacts of FISTA and SURE-IT. The VDAMP errors are biased because of the additional gradient step in line 11 of Algorithm 1

power spectrum of the signal, and highlights the benefit of modeling the aliasing as colored. Fig. 4 shows  $\mathbf{x}_0$ , the ground truth Fourier coefficients  $\mathbf{y}_0$ , and FISTA, SURE-IT, VDAMP- $\alpha$  and VDAMP-S reconstructions for uniform sampling at  $k = 50$ , with entry-wise errors  $|\hat{\mathbf{x}} - \mathbf{x}_0|$ .

For two-level and polynomial sampling the variable density distribution partially compensates for the power spectrum of the signal, so the aliasing is less strongly colored. Fig. 2b and Fig. 2c show that this leads to a less substantial but still significant improvement in convergence speed for VDAMP- $\alpha$  and VDAMP-S. There is an NMSE improvement in VDAMP-S over VDAMP- $\alpha$ , which indicates that VDAMP-S's  $c_k$  update successfully leads to a  $\tilde{\mathbf{r}}_k$  with lower NMSE than VDAMP- $\alpha$ . The performance of VDAMP- $\alpha$  in these figures also highlights that VDAMP can converge to an estimate with a higher NMSE than FISTA, despite the richer regularization. This is due to the  $\mathbf{P}^{-1}$  scaling in the gradient step, line 4 of Algorithm 1, which effectively increases the measurement noise for coefficients sampled with low probability.

In our implementation the mean per-iteration compute time over all experiments was 0.15s for FISTA, 0.16s for SURE-IT, 0.18s for VDAMP- $\alpha$  and 0.20s for VDAMP-S. The small additional computational cost of SURE-IT over FISTA is due to the calculations required for threshold selection with SURE. The further per-iteration cost of VDAMP is due to the  $1 + 3s$  inner products required for the  $\tau_k$  update in line 7 of Algorithm 1, and in the case of VDAMP-S, the  $1 + 3s$  inner products required for updating  $c_k$  by (26). Despite the additional per-iteration computational cost, the effectiveness of the denoiser  $\mathbf{g}(\mathbf{r}_k; \tau_k)$  significantly reduces the required

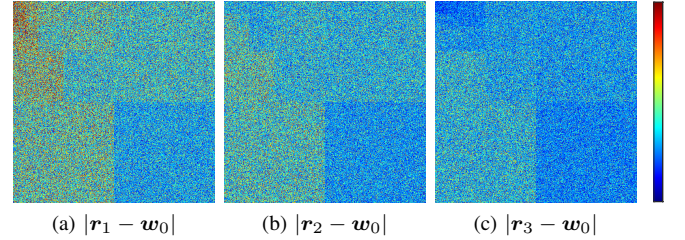


Fig. 5: The magnitude of the effective noise for VDAMP-S for a Shepp-Logan undersampled with the polynomial mask of Fig. 3c for iterations  $k = 1, 2, 3$ , where the colormaps are on the same scale. The logarithm is not shown, unlike Fig. 1f.

computation time. For instance, the time required to reach an NMSE of -35dB in Fig. 2a was 406s for FISTA, 105s for SURE-IT, 3.6s for VDAMP- $\alpha$  and 3.4s for VDAMP-S, and in Fig. 2b was 12s for FISTA, 11s for SURE-IT, 2.5s for VDAMP- $\alpha$  and 2.0s for VDAMP-S.

#### E. Empirical evidence of state evolution

This section presents empirical evidence that VDAMP obeys the colored state evolution given by (7), using the illustrative case of VDAMP-S with polynomial sampling at  $N/n = 12$ , as in Fig. 3c. In Fig. 5,  $|\mathbf{r}_k - \mathbf{w}_0|$  is shown for  $k = 1, 2, 3$ , indicating that the unbiased subband-dependant effective noise structure shown at  $k = 0$  in Fig. 1 is preserved. For  $k = 1, 5, 20$ , Fig. 6 shows quantile-quantile plots against a Gaussian of the three illustrative subbands of  $\mathbf{r}_k - \mathbf{w}_0$ : the diagonal detail at scale 1, the horizontal detail at scale 2 and the vertical

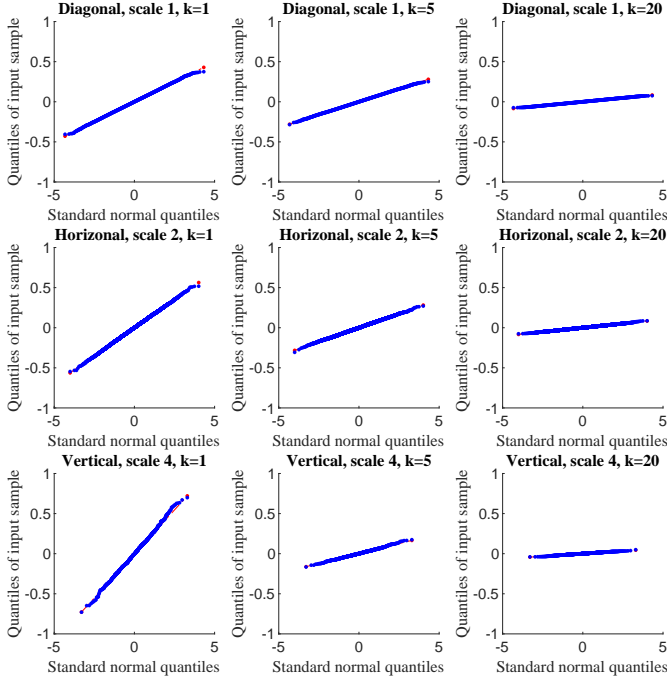


Fig. 6: Normalized quantile-quantile plots against a Gaussian for three subbands of VDAMP-S's  $r_k - w_0$  for  $k = 1, 5, 20$  for polynomial sampling with  $N/n = 12$  in blue, and points along a straight line in red. The real part is plotted in the top and bottom rows and the imaginary is plotted in the middle row. Linearity of the blue points indicates that the data comes from a Gaussian distribution, and the decreasing gradient shows that the variance decreases with increasing  $k$ . Finite dimensional effects causing small deviations from an exact Gaussian are more apparent at coarse scales, where the dimension is smaller.

detail at scale 4, where scale 1 is the finest and scale 4 is the coarsest. The linearity of the blue points provides evidence that the effective noise is Gaussian, so that VDAMP has the effective noise given by (7) and (8).

#### IV. CONCLUSIONS

Based on the observation that Fourier sampling from a non-uniform spectral density leads to colored aliasing, we propose VDAMP, an algorithm based on OAMP that obeys a colored state evolution. State evolution provides an effective way to tune model parameters via SURE, implying that a single algorithm can be used for arbitrary variable density scheme without the need for manual adjustment. More degrees of freedom are feasibly allowed in the model, enabling higher order prior information such as anisotropy, variability across scales and structured sparsity, without the need to estimate the structure a priori such as in model-based compressed sensing [2].

VDAMP was motivated by the application of compressed sensing to accelerated MRI. Developments are required for VDAMP to be applicable to MRI data, which is acquired across a number of coils that possess a sensitivity profile [22], [31]. Further developments are required for VDAMP to be

applicable to Fourier sampling with 1D readout curves, where elements of  $\Omega$  are generated dependently.

It is known that the state evolution of OAMP holds for a wide range of denoisers  $g(r_k; \tau_k)$  [25], [40]. In [1], a number of standard compressed sensing algorithms that leverage image denoisers designed for Gaussian noise were shown to perform well on MRI reconstruction tasks, despite the mismatch between the aliasing and its model. A sophisticated denoiser equipped to deal with wavelet coefficients corrupted with known colored Gaussian noise would be expected to perform well in conjunction with VDAMP.

#### REFERENCES

- [1] R. AHMAD, C. A. BOUMAN, G. T. BUZZARD, S. CHAN, E. T. REEHORST, AND P. SCHNITER, *Plug and play methods for magnetic resonance imaging*, (2019), <http://arxiv.org/abs/1903.08616>.
- [2] R. G. BARANIUK, V. CEVHER, M. F. DUARTE, AND C. HEGDE, *Model-Based Compressive Sensing*, IEEE Transactions on Information Theory, 56 (2010), pp. 1982–2001, <https://doi.org/10.1109/TIT.2010.2040894>, <http://ieeexplore.ieee.org/document/5437428/>.
- [3] M. BAYATI, M. LELARGE, AND A. MONTANARI, *Universality in polytope phase transitions and message passing algorithms*, The Annals of Applied Probability, 25 (2015), pp. 753–822, <https://doi.org/10.1214/14-AAP1010>, <http://projecteuclid.org/euclid.aop/1424355130>.
- [4] M. BAYATI AND A. MONTANARI, *The Dynamics of Message Passing on Dense Graphs, with Applications to Compressed Sensing*, IEEE Transactions on Information Theory, 57 (2011), pp. 764–785, <https://doi.org/10.1109/TIT.2010.2094817>, <http://ieeexplore.ieee.org/document/5695122/>.
- [5] A. BECK AND M. TEOULLE, *A Fast Iterative Shrinkage-Thresholding Algorithm for Linear Inverse Problems*, SIAM Journal on Imaging Sciences, 2 (2009), pp. 183–202, <https://doi.org/10.1137/080716542>, <http://epubs.siam.org/doi/10.1137/080716542>.
- [6] F. CALTAGIRONE, L. ZDEBOROVA, AND F. KRZAKALA, *On convergence of approximate message passing*, in 2014 IEEE International Symposium on Information Theory, IEEE, 6 2014, pp. 1812–1816, <https://doi.org/10.1109/ISIT.2014.6875146>, <http://ieeexplore.ieee.org/lpdocs/epic03/wrapper.htm?arnumber=6875146>.
- [7] E. CANDÈS, J. ROMBERG, AND T. TAO, *Robust uncertainty principles: exact signal reconstruction from highly incomplete frequency information*, IEEE Transactions on Information Theory, 52 (2006), pp. 489–509, <https://doi.org/10.1109/TIT.2005.862083>, <http://ieeexplore.ieee.org/document/1580791/>.
- [8] N. CHAUFFERT, P. CIUCIU, AND P. WEISS, *Variable density compressed sensing in MRI. Theoretical vs heuristic sampling strategies*, Proceedings - International Symposium on Biomedical Imaging, (2013), pp. 298–301, <https://doi.org/10.1109/ISBI.2013.6556471>.
- [9] D. DONOHO, *Compressed sensing*, IEEE Transactions on Information Theory, 52 (2006), pp. 1289–1306, <https://doi.org/10.1109/TIT.2006.871582>, <http://ieeexplore.ieee.org/document/1614066/>.
- [10] D. DONOHO, *How High-Dimensional Geometry is Transforming the MRI Industry*, 2017, <https://vimeo.com/225634059>.
- [11] D. L. DONOHO AND I. M. JOHNSTONE, *Adapting to Unknown Smoothness via Wavelet Shrinkage*, Journal of the American Statistical Association, 90 (1995), pp. 1200–1224, <https://doi.org/10.1080/01621459.1995.10476626>, <http://www.tandfonline.com/doi/abs/10.1080/01621459.1995.10476626>.
- [12] D. L. DONOHO, A. MALEKI, AND A. MONTANARI, *Message-passing algorithms for compressed sensing*, Proceedings of the National Academy of Sciences of the United States of America, 106 (2009), pp. 18914–9, <https://doi.org/10.1073/pnas.0909892106>, <http://www.ncbi.nlm.nih.gov/pubmed/19858495>, <http://www.pubmedcentral.nih.gov/articlerender.fcgi?artid=PMC2767368>.
- [13] E. M. EKSIOGLU AND A. K. TANC, *Denoising AMP for MRI Reconstruction: BM3D-AMP-MRI*, SIAM Journal on Imaging Sciences, 11 (2018), pp. 2090–2109, <https://doi.org/10.1137/18M1169655>, <https://epubs.siam.org/doi/10.1137/18M1169655>.
- [14] Y. C. ELДАР, *Generalized SURE for Exponential Families: Applications to Regularization*, IEEE Transactions on Signal Processing, 57 (2009), pp. 471–481, <https://doi.org/10.1109/tsp.2008.2008212>, <http://dx.doi.org/10.1109/TSP.2008.2008212>.

